Optimizing Thermal Energy Harvesting in Few-Layer MoS2 with Measurements of Electron's Effective Mass in Two-Dimensional Semiconductors

Kuan-Cheng Lu,[1,‡] *Chetan Awasthi,*[1,2,‡] *Ta-Wei Chiu,*[1] *S. S. Islam,*[2,*] *Kimitoshi Kono,*[1,3] *Wen-Bin Jian,*[1,*] *Kazuhito Tsukagoshi* [1,4]

[1] Department of Electrophysics, National Yang Ming Chiao Tung University, 1001 University Road, Hsinchu 300093, Taiwan

[2] Centre for Nanoscience and Nanotechnology, Jamia Millia Islamia (A Central University), Jamia Nagar, New Delhi-110025, India

[3] International College of Semiconductor Technology, National Yang Ming Chiao Tung University, 1001 University Road, Hsinchu 300093, Taiwan

[4] International Center for Materials Nanoarchitectonics (WPI-MANA), National Institute for Materials Science (NIMS), Tsukuba, Ibaraki 305-0044, Japan

‡ These authors contributed equally to this work.

* Corresponding Authors: S. S. Islam and Wen-Bin Jian.

KEYWORDS: Two-Dimensional Semiconductors, Seebeck Coefficient, Power Factor, Memory Step, MoS_2, Mott's Hopping Transport, Electron Transport

ABSTRACT. The ultrathin two-dimensional semiconductor of MoS_2 demonstrates prominent field-effect performances and is the best candidate for down-sizing transistors. Its electron transport and thermoelectric properties have been explored only in a few layers of MoS_2 or at low temperatures, and the interrelation between the electrical and thermoelectric properties has not been studied yet. We fabricate thermoelectric and field-effect transistor devices with MoS_2 thicknesses ranging from 1 to 39 layers and carry out electrical and thermoelectric property measurements in a wide temperature range from 80 to 600 K. Mott's hopping transport, thermal activation, and phonon scattering theories in electrical and thermoelectric properties are simultaneously and systematically investigated. Temperature behaviors and carrier concentration dependences are drawn and described in detail. Moreover, Seebeck coefficients, conductivities, and thermoelectric power factors are sketched as a function of MoS_2 flake thickness (number of layers). We point to the high Seebeck coefficient and the power factors for MoS_2 flakes with thicknesses of less than 20 layers, revealing the best candidate for thermopower applications among all two-dimensional semiconductors. In addition, we probe the extrinsic effect of memory steps due to trapped charges at temperatures above 450 K in the modulation of electron transports and thermoelectric properties. The extrinsic effect of trapped charges in the substrate presents promising applications as high-temperature thermal sensors.

INTRODUCTION

The history and developments of the thermoelectric (TE) field have been detail illustrated in the review article authored by Mildred Dresselhaus et al. [1]. The TE field drew much attention in the 1950s for the discovery of three-dimensional TE bulk materials and niche applications [1,2]. It was followed by the definition of a dimensionless figure of merit [3] and the exploration of materials of a high TE figure of merit, such as bismuth telluride with related materials and

SiGe alloys. It triggered, as well, the seeking of phonon-glass electron-crystal materials [1,4] such as TE clathrates [4]. The essential parameter of TE materials is the Seebeck coefficient (S), which offers the output voltage of harvested energy. The Seebeck coefficient (S) is enhanced with excessive density of states near the Fermi level [5,6] that exists in low-dimensional and nanostructured materials. As a result, low-dimensional TE materials, including quantum wells, nanowires, quantum dots, and agglomerated low-dimensional materials, like nanocomposite and nanostructured TE materials, have drawn much attention in the past two decades [1,2,7,8]. In addition to the Seebeck coefficient (S), another essential parameter, the power factor ($PF = S^2\sigma$), where σ is conductivity, offers the output power as well as the current of harvested energy. In recent studies, it was addressed that increasing the PF is a better strategy to boost power generation for a given figure of merit [9].

The unearthing of graphene [10] initiated the exploration of the highest potential low-dimensional materials, the two-dimensional (2D) semiconductors [11,12], for mass production and feasible employment, especially for semiconductor technologies. Among most 2D semiconductors, MoS_2 exhibited relatively high device manufacturing stability and was more thoroughly studied [11,13,14]. It has been demonstrated to exhibit high on-current, on/off ratio, and mobility with a low subthreshold swing for single-layer MoS_2 field-effect transistors (FETs) [11,15]. To achieve complementary FET operations, natively *n*-type and multilayer MoS_2 flakes were chemically doped and converted to *p*-type devices [16]. It was demonstrated to reduce the MoS_2 channel length to sub-100 nm and to push an on-current approaching 1 mA/μm [17]. Crested FETs fabricated with rippled MoS2 sheets placed on crested and corrugated SiN_x substrates presented boosting of carrier mobility up to two orders of magnitude under ambient conditions [18,19]. In addition to device performance, monolayer MoS_2 flakes exhibited a metal-insulator transition due to strong

Coulomb interactions in the two-dimensional electron system [20] and, with an increasing carrier density, multilayer MoS_2 flakes presented a superconducting phase at temperatures lower than 10 K [21].

In addition to intrinsic MoS_2 properties for the FET applications, other demonstrations used heterostructures with extrinsic features, such as the nonvolatile memory device with a floating gate device structure [22]. Moreover, the extrinsic effect of trapping charges between the MoS_2 and the metal gate led to memory steps in transfer curves at temperatures above 450 K [23] and to hysteresis loops and thermally assisted memory effects [24,25]. On the other hand, MoS_2 exhibited promising TE properties such as a high photothermoelectric Seebeck coefficient (S) of 20 mV/K in a single-layer flake [26] and a remarkably large TE power (S) of 30 mV/K in a chemical-vapor-deposition grown single-layer film at 280 K [27]. It was theoretically predicted to have a large TE power factor of 28 mW/m K^2 in a suspended single-layer MoS_2 [28]. In previous experimental results, the TE power factor of few-layer MoS_2 was estimated to be as large as 5 mW/m K^2 in the on state in the bilayer flake [29] and approaching 8.5 mW/m K^2 in the metallic region in the bilayer flake [30]. Most interestingly, an anomalous carrier sign change at low temperatures, a Kondo-like behavior and band hybridization of MoS_2/h-BN heterostructure were recently studied. A positive TE power (S) of ~2 mV/K and a TE power factor of ~50 mW/m K^2 were obtained at temperatures below 50 K [31].

Although the emergence of hopping transport in TE power and conductance of single-layer MoS_2 was experimentally studied, the relation between the disorder parameter of the hopping transport and the TE power has not been investigated yet. Nor did the conduction mechanism at high temperatures be studied regarding to the TE power. In addition, the TE power factor was essential for the TE applications, but its temperature, layer thickness, and carrier concentration dependences were not completely explored. On the other hand, the extrinsic effect of the memory step was observed at temperatures above 450 K, but the effect on the TE power has not yet been inspected. In this work, we explored MoS_2 with a thickness from a single layer up to 40 layers on the TE power and TE power factor in a wide temperature range from 80 to 600 K. We discovered enhanced TE power and temperature sensing capabilities due to memory steps at very high temperatures.

RESULTS AND DISCUSSIONS

MoS_2 flakes are isolated from the bulk counterpart and placed on Si wafers capped with a 300-nm thick SiO_2 layer. For MoS_2 flakes with a thickness of less than 6 layers, the differences in optical contrast between the substrate and the flakes are adopted to determine the flake thicknesses, as shown and discussed in **Fig. S1** in the **Supporting Information**. The thicknesses of those thick flakes are determined using an atomic force microscope (AFM). MoS_2 flakes are patterned with Au metal electrodes to form a simultaneous TE and field-effect transistor (FET) device. **Figure 1a** presents a top view of a TE-FET device with Au electrodes marked by numbers. Electrodes 1 and 2 are source and drain electrodes for measuring field-effect properties. Device parameters, including field-effect performances of several typical MoS_2 TE-FET devices, are listed in **Table S1** in the **Supporting Information**. The thicknesses of those TE-FET devices range from 1 to 39 layers, and the mobilities and on-currents of all devices are high enough that the issue of contact resistance can be ignored. In addition, Electrodes 1 and 2 are also used as temperature sensors and for detecting spatial TE voltage variations. Electrode 3 is a micro heater driven by an alternating current (AC) voltage at the frequency of 6.85 Hz. The measurements of temperature differences between Electrodes 1 and 2 are described in detail in the discussion of **Fig. S2** in the **Supporting Information**. The TE voltage is obtained using the standard 2ω method (see Experimental

Section). The electrical connection and measurement of the TE properties of TE-FET devices are provided in **Fig. 1b**, where the heavily doped Si substrate is used as a back-gating electrode to adjust the carrier concentration as well as the Fermi level of the MoS_2 channel.

Figure 1c shows transfer curves of Devices M1 and M5 with thicknesses of 1 and 2 layers, revealing typical electron-contributed, n-type FET behaviors, on-currents of 8.49 and 2.80 $\mu A/\mu m$ at the back gating voltage (V_{BG}) of 60 V, and on/off ratios of 3.6×10^7 and 1.2×10^7. The inset to **Fig. 1c** gives a linear source-drain current-voltage (J_{DS}-V_{DS}) behavior, indicating an Ohmic contact between the MoS_2 channel and the Au metal electrodes. Our previous work has investigated the FET performance of few-layer MoS_2 flakes in detail [13]. It is discovered that, due to different degrees of intrinsic disorders, the MoS_2 FETs present an insulating state that can be analyzed using the 2D Mott's variable range hopping (VRH) conduction [32, 13] at low temperatures. Here, we focus on disorder effects on the TE-FET devices and investigate devices of MoS_2 flakes with either intrinsic or extrinsic disorders. On the other hand, **Fig. 1c** shows the steepest ascending dotted line and the horizontal dashed line with the intersection at V_{BG} of about -34.7 V, which gives the turn-on V_{BG} (denoted as V_x) of electron doping in the MoS_2 channel [14]. The native electron doping concentration (n_e) of Device M1 is estimated to be 2.34×10^{12} cm^{-2} according to the form of $n_e = C_{ox}(0 - V_x)/q$ [14], where C_{ox} of about 1.15×10^{-8} F cm^{-2} is the areal capacitance of the SiO_2 dielectric layer. Such a high native doping concentration points to a degenerated semiconductor in 2D MoS_2 flakes. **Figure 1d** presents corresponding Seebeck coefficients as a function of V_{BG} for Devices M1 and M5. The Seebeck coefficient is negative, confirming again the electron doping at high, positive V_{BG} with the n-type TE-FET switched on. The negative Seebeck coefficient of Device M1, following the trend of transfer curves in **Fig. 1c**, goes up to the maximum of 281 $\mu V/K$

at V_{BG} of -12 V (denoted as V_{peak}). According to the Cutler-Mott theory [6], the Seebeck coefficient (S) of degenerated semiconductors is described as:

$$S = -(\pi^2 k_B^2 T/3q)(d \ln G\, /dE)_{E=E_F}, \tag{1}$$

where k_B is the Boltzmann constant, T is temperature, G is conductance, q is charge, and E is the energy of charge carriers [6]. The term of the derivative of $\ln G$ with respect to E in Eq. (1) can be rewritten as $(d \ln G/dV_{BG})(dV_{BG}/dE)_{E=E_F}$ [33]. The data of $(d \ln G/dV_{BG})$ of Device M1 are presented as black open circles in **Fig. 1d**. A large shift between the $(d \ln G/dV_{BG})$ and the Seebeck coefficient is identified, implying an extrinsic effect such as additional charges of interface trap states in the interface between the MoS_2 flakes and the SiO_2 dielectric layer.

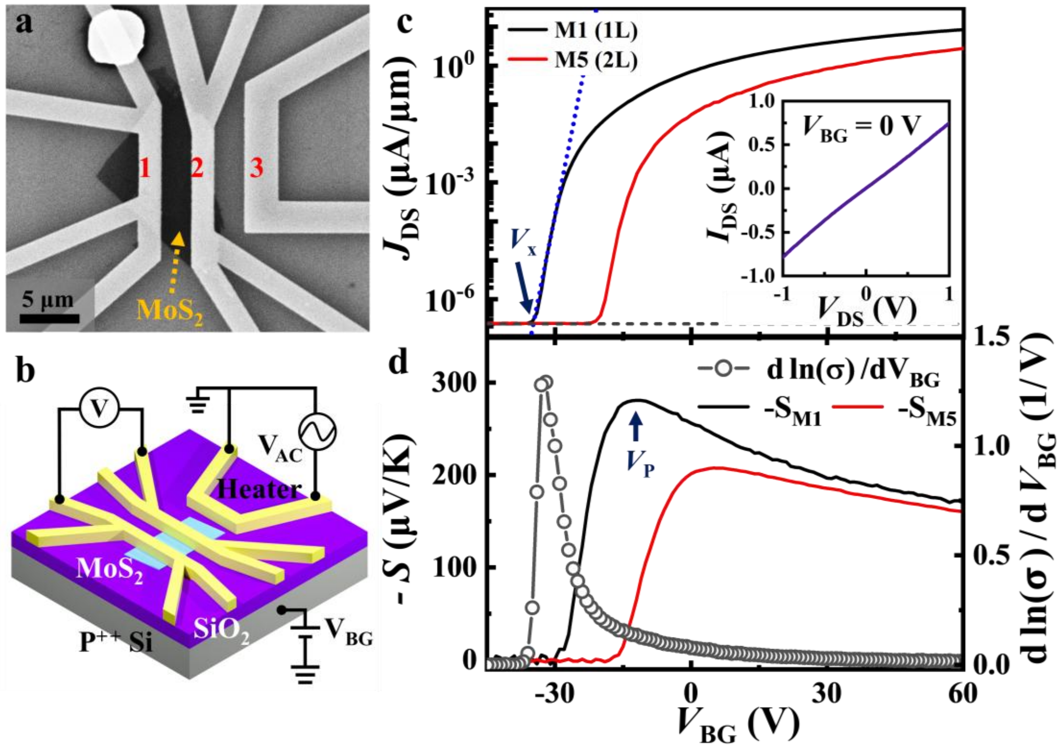

Figure 1. (a) Scanning electron microscope (SEM) image of a typical monolayer MoS_2 TE-FET device (Device M1). Electrodes 1 and 2 are used as source and drain electrodes and are employed as thermometers. Electrodes 1 and 2 are given to measure the thermovoltage across

themselves. Electrode 3 is a heater that offers sinusoidal heat flux. (b) Scheme of the MoS_2 TE-FET device with an electrical circuit for TE measurements. The substrate is offered as a back-gating electrode, and a lock-in amplifier is implemented to conduct thermovoltage measurements. (c) Transfer curves of Devices M1 and M5 with thicknesses of 1 and 2 layers at room temperature. The inset offers a current-voltage (I-V) curve of Device M1. (d) Seebeck coefficients as a function of back gating voltage (V_{BG}) for Devices M1 and M5. The extreme Seebeck coefficient of 281 $\mu V/K$ (207 $\mu V/K$) exists at V_{peak} of -12 V (+4 V) for Device M1 (M5). The open circles delineate data of $d(\ln G)/dV_{BG}$ of Device M1.

Figure 2 presents complete information on Seebeck coefficients as a function of V_{BG} at temperatures ranging from 120 to 600 K. Like mono- and bi-layer MoS_2 flakes, Device M6 of three layers in thickness shows a nonzero thermopower started from V_{BG} of -33 V (see **Fig. 2a**) at 300 K. The thermopower increases with increasing V_{BG} up to the maximum value of ~281 $\mu V/K$ at V_{BG} of 6 V. The magnitude of the thermopower then decreases with a further increase of V_{BG} due to an increase of electron carrier concentration that will be discussed in the following paragraphs as well as in the **Supporting Information**. When the temperature is raised up to 600 K, the extreme thermopower boosts up to ~698 $\mu V/K$. In contrast, the maximum thermopower decreases to be about 69.8 $\mu V/K$ at 120 K. The temperature behavior, correlating to 2D Mott's VRH and metallic conduction, will be separably discussed later for **Figs. 3** and **4**. Particularly, a small downward step (marked as a step in **Fig. 2a**) on the Seebeck coefficient is commonly perceived in few-layer MoS_2 devices at temperatures higher than 450 K, whereas it is hardly observed for TE-FETs of very thick MoS_2 flakes. We will also provide comprehensive discussions about the marked step later.

In **Fig. 2b**, another example of the MoS_2 TE-FET (Device M1) exposes the same feature as that displayed in **Fig. 2a**. The thermopower is turned on, consistent with the field-effect behavior of the n-type FET. Additionally, we point out that the V_{peak} at the extremum of the thermopower varies with temperature. The V_{peak} moves to further negative voltages with an increase in temperature. The temperature-dependent V_{peak} is accordingly displayed in **Fig. 2c**. To explore the mechanism further, the $V_x's$ of the turn-on of the field-induced electron doping are offered in **Fig. 2c**, as well, for comparison. It is noted that the V_{peak} adequately follows the temperature behavior of the V_x. The V_x moves to lower voltages at higher temperatures, indicating de-trapping of the interface trapped states in the interface between the MoS_2 flakes and the SiO_2 dielectric layer [24, 34]. The result corroborates our previous conjecture about the extrinsic disorder and scattering effect from the supporting substrate. On the other hand, the temperature behavior of the thermopower at V_{BG} of 60 V is drawn in **Fig. 2d**. At temperatures lower than 180 K, the temperature-dependent thermopower is proportional to $T^{1/3}$ while it linearly follows T above 300 K. In particular, the thermopower of the 2D MoS_2 TE-FETs always increases with the increasing temperature at all $V_{BG}'s$ (see **Fig. 2a**).

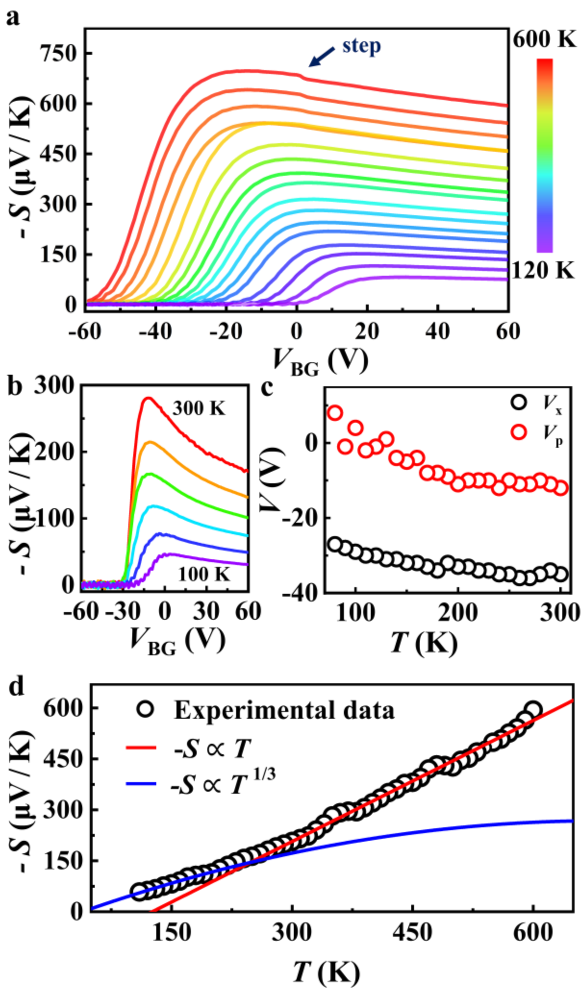

Figure 2. (a) Seebeck coefficients of the trilayer MoS$_2$ TE-FET device (Device M6) as a function of V_{BG} at temperatures ranging from 120 to 600 K. (b) Seebeck coefficients of the monolayer MoS$_2$ TE-FET device (Device M1) at temperatures of 100, 140, 180, 220, 260, and 300 K. (c) V_{peak} and V_x of Device M1 as a function of temperature. (d) The Seebeck coefficient as a function of temperature (T) at V_{BG} of 60 V. The red line shows the best linear least-square fitting in the temperature range from 300 to 600 K, and the blue line presents the best least-square fitting to $T^{1/3}$ in the temperature range from 120 to 200 K.

To explore the mechanism of thermopower in 2D MoS_2, we investigate thermoelectric properties in correlation with electron transport, and we study as a first step in the temperature range at which the 2D Mott's VRH conduction dominates. The 2D Mott's VRH conduction describes that the resistivity of the 2D channel (ρ_{2D}) varies with temperature T according to the form of $\rho_{2D} \propto \exp\left((T_0/T)^{1/3}\right)$, where T_0 is the disorder parameter [32]. **Figure 3a** presents the hopping behavior and the best least-square fitting lines at temperatures ranging from 80 to 180 K. The resistivity suitably follows the 2D hopping conduction when the channel is turned on at V_{BG} above 0 V. Moreover, the disorder parameters $T_0's$ are estimated from the linear least-square fittings in **Fig. 3a**. In the same temperature range, the thermopower S depends on T in line with the equation of $S(T) \propto T^{\frac{d-1}{d+1}}$, where $d = 2$ is the dimension of the electron system [35,32]. **Figure 3b** presents the linear behavior between the negative Seebeck coefficient $-S$ and $T^{1/3}$. The range of temperatures within which the fitting obeys well follows the same temperature range in **Fig. 3a**, indicating the contribution from the disorder effect. **Figure 3c** presents the $T_0^{1/3}$ and $-S$ as a function of the logarithm of the carrier concentration ($\ln(n_{2D})$), showing a linear dependent feature at carrier concentrations ranging from 2.27×10^{12} to 6.58×10^{12} cm^{-2}. The resistivity ρ_{2D} is inversely proportional to the carrier concentration n_{2D} and, it is also proportional to $\exp\left((T_0/T)^{1/3}\right)$ due to the disorder effect. Thus, the $T_0^{1/3}$ is proportional to $\ln(n_{2D})$ in the same temperature range. On the other hand, the Seebeck coefficient S at the constant temperature of 180 K is also proportional to $C + \ln(n_{2D})$ [36], where C is a constant. The result corroborates the same mechanism of the disorder effect, and it indicates the same relationship to the 2D carrier concentration n_{2D}.

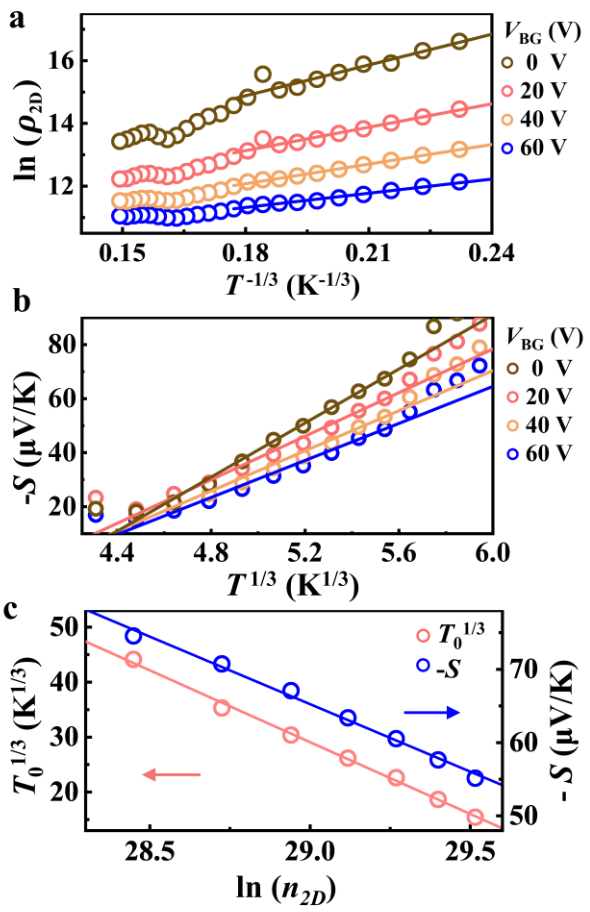

Figure 3. (a) $\ln(R)$ as a function of $T^{-1/3}$ of Device M4 at various V_{BG}'s in the temperature range from 80 to 300 K. The solid lines provide the best linear least-square fitting results over the temperature range from 80 to 180 K. (b) Seebeck coefficients versus $T^{1/3}$ at V_{BG}'s of 0, 20, 40, and 60 V over the temperature range from 90 to 200 K. The solid lines give the best linear least-square fittings to the data over the temperature from 90 to 180 K. (c) Disorder parameter ($T_0^{1/3}$) and Seebeck coefficients as a function of n_{2D} in a logarithmic scale. The T_0's are obtained from linear fittings in **Fig. 3b**, and the Seebeck coefficients are taken at 180 K.

As expected, the disorder effect may disappear under the circumstances of a high thermal energy. When the temperature increases above 300 K, and the channel is turned on at V_{BG} above 0 V, the electron transport exhibits thermally activated transport, which is always observed in connection with the 2D hopping conduction at low temperatures. **Figure 4a** reveals the thermally activated behavior described by the form of $\rho_{2D} \propto \exp(E_A/k_BT)$, where E_A is the activation energy. The fitting lines indicate that the temperature dependence of resistance exactly follows the thermally activated transport in the temperature range from 330 to 460 K. Through the linear least-square fitting, the activation energy E_A is estimated. At temperatures above 460 K, the resistance behavior changes remarkably. We present the same data in a linear scale in **Fig. S3** of the **Supporting Information**. The temperature dependence of resistance is linearly dependent on temperature, which signifies the phonon scattering and the metallic state above 460 K. The electron transport changes from 2D Mott's hopping with thermally activated transport to the metallic state, presenting an interesting metal-to-insulator transition [20].

The corresponding Seebect coefficients as a function of temperature are unveiled in **Fig. 4b**. The Seebeck coefficient is just linearly dependent on temperature without any perceivable transition in the whole temperatures ranging from 300 to 600 K. Usually, the Seebeck coefficient will decrease with an increase of temperature if the thermopower follows the electron transport of thermal activation [36]. In all the devices of MoS_2 TE-FET, the decrease of the Seebeck coefficient with an increase in temperature has never been noticed yet (see, for example, **Fig. 2d**). The disappearance of the decreasing thermopower could be attributed to the enhanced phonon scattering at high temperatures that dominates the electron diffusion in the generation of thermopower. To explore about the electron transport and the thermopower, we present the activation energy E_a and the logarithm of the Seebeck coefficient $\ln(|S|)$ varied with the carrier concentration n_{2D} in **Fig. 4c**. The resistivity ρ_{2D} is inversely proportional to the carrier concentration n_{2D} and it is proportional to $\exp(E_A/k_BT)$, thus the E_a is proportional to $\ln(n_{2D})$ at the same temperature. In addition, the Seebeck coefficient at a constant temperature is proportional to $n_{2D}^{-2/3}$ according to the theory for nearly free electrons [37]. Consequently, we investigate the reliance between the $\ln(|S|)$ and the $\ln(n_{2D})$, and it reveals the linear manner at carrier concentrations ranging from 2.41$\times 10^{12}$ to 6.72$\times 10^{12}$ cm^{-2}. The $n_{2D}^{-2/3}$ behavior at high carrier concentrations ($V_{BG} > V_{peak}$) infers the depression of thermopower and thermally induced carrier diffusion due to more charge carriers compacted in the channel. On the other hand, we shall consider both effects presented in **Figs. 3c** and 4c to investigate the dependence of the Seebeck coefficient on the back gate voltage (V_{BG}) such as those shown in **Fig. 1d**. The V_{BG} behavior of the thermopower is displayed in **Fig. S4** in the **Supporting Information**. The thermopower is separately fitted at either a lower carrier concentration ($V_{BG} < V_{peak}$) or a higher carrier concentration ($V_{BG} > V_{peak}$) according to the carrier concentration behaviors revealed in **Figs. 3c** and **4c**. The details are expressed in the discussion of **Fig. S4,** and, particularly, the fitting results lead to evaluating the universal constant of k_B/q and the carrier effective mass of 0.1 m_0, where k_B is the Boltzmann constant, q is the charge, and m_0 is the mass of the electron. The results of the extracted values in line with theories and other group's experiments that corroborate the robustness of our accurate and precise thermopower measurements in the TE-FETs.

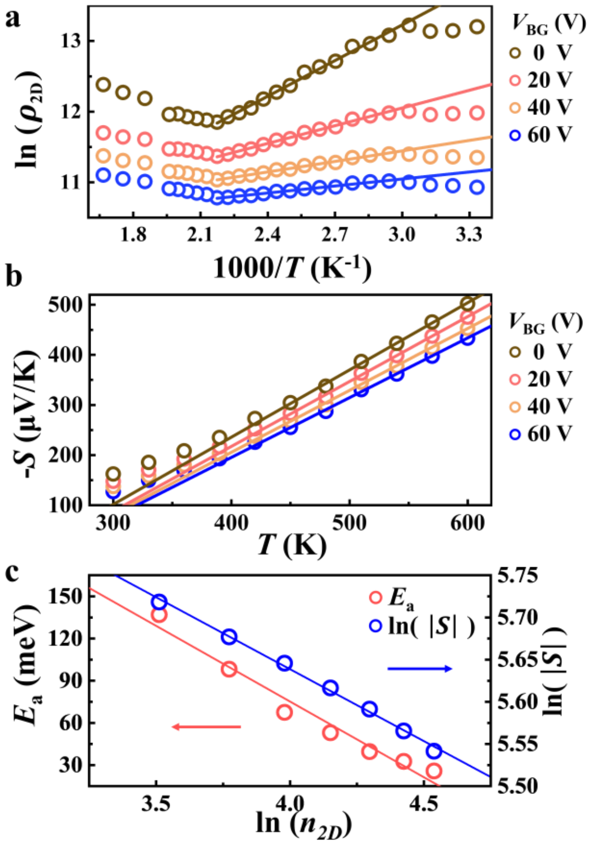

Figure 4. (a) $\ln R$ versus $1000/T$ at temperatures ranging from 300 to 460 K. The solid lines display the best linear least-square fittings. (b) Seebeck coefficients versus T of Device M7 at various V_{BG}'s over the temperature range from 300 to 600 K. The solid lines represent the best linear least-square fittings at temperatures ranging from 330 to 460 K. (c) Activation energy (E_a) and Seebeck coefficients as a function of V_{BG}. The E_a's are obtained from fittings in **Fig. b** and the Seebeck coefficients are measured at 450 K.

In previous paragraphs, we point out an extrinsic effect due to interface trapped charges between the MoS_2 flake and the SiO_2 substrate according to the shift between the field-effect and the thermopower behaviors in **Fig. 1d** and the step designated in **Fig. 2a**. We will then investigate deeply into the extrinsic effect. The inset to **Fig. 5a** reveals the back-gating behavior of the Seebeck coefficients for Device M7 at temperatures above 300 K. A clear step is probed in the V_{BG} dependent thermopower at 600 K, like that marked in **Fig. 2a** for Device M6. To multiply the effect, we expose the dS/dV_{BG} as a function the V_{BG} in **Fig. 5a**. The differential of the Seebeck coefficient exhibits a peak close to the V_{BG} of 0 V. The peak at zero back-gating voltage indicates the trapping and detrapping due to the extrinsic effect of trapped charges in the SiO_2 substrate. In particular, the differential of the Seebeck coefficient is extremely sensitive to the ambient temperature. In addition to the thermopower, the V_{BG} dependent currents at temperatures above 300 K reveal a similar behavior that a step feature is observed in the curve at 600 K in the inset to **Fig. 5b**. The results are consistent with those reported in the literature [24] in which a mode of trapped states in the dielectric is proposed to explain the trapping (injection) of electrons at negative V_{BG} as well as the detrapping of electrons at positive V_{BG}. We plot the transconductance as a function of the V_{BG} in **Fig. 5b** to expose its sensitive temperature dependency. At temperatures above 480 K, the transconductance exposes the peak near the V_{BG} of 0 V, indicating the trapping and detrapping of charges in the SiO_2 substrate with a very low positive or negative V_{BG}.

We further dig into the current's dependence on the back-gating voltage, V_{BG}. In **Fig. S5** in the **Supporting Information**, the analysis of the trapped carrier concentration for Device M7 at 600 K is sketched and described in detail. Through the shifted behavior of the linear current-V_{BG} manner above and below the V_{BG} of 0 V, the trapped carrier concentration is evaluated to be $\sim 6.84 \times 10^{11}$ cm^{-2}, which is very close to that estimated in the previous report [24]. The release of the trapped electrons causes an increase in conductivity and current by up to ~45%. In contrast, it generates a decrease of the Seebeck coefficient from 522 to 509 $\mu V/K$, about a 2.5% reduction. The power factor is calculated using $PF = S^2\sigma$, where σ is the conductivity, and the release of the trapped electrons causes a rise of power factor of ~38%. To integrate information from insets to

Figs. 5a and **5b**, the carriers released from the additional gating of extrinsic trapping charges in the SiO₂ contribute to an increase of channel current and a decrease of thermopower simultaneously when the gating voltage V_{BG} is slightly biased to a low positive voltage. On the other hand, the sensitive temperature dependences of the differential of the thermopower (**Fig. 5a**) and transconductance (**Fig. 5b**) are quantitatively portrayed in **Fig. 5c**. It is crystal clear to distinguish the strong temperature dependency at temperatures above 450 K. The extrinsic effect due to the trapping charges in the SiO₂ plays an important role in applying to high-temperature thermal sensors.

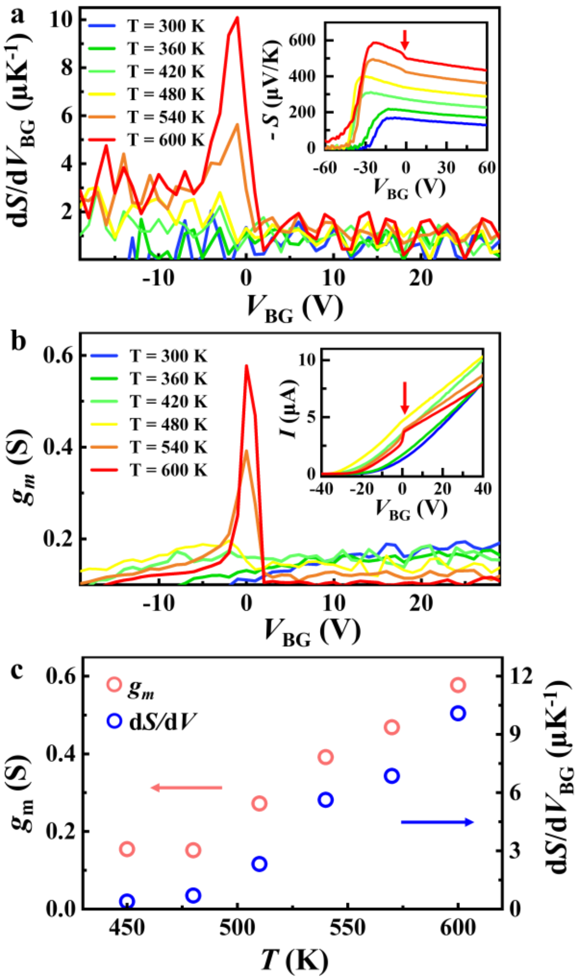

Figure 5. (a) Differential Seebeck coefficients as a function of V_{BG} of trilayer MoS_2 TE device (Device M7) at various temperatures. The inset displays corresponding Seebeck coefficients versus V_{BG} with an arrow pointing out a steep variation near V_{BG} of 0 V at temperatures above 450 K. (b) Transconductances as a function of V_{BG}. The inset provides current as a function of V_{BG} with an arrow indicating a sharp change near V_{BG} of 0 V. (c) Transconductances and differential Seebeck coefficients at V_{BG} of 0 V at temperatures from 450 to 600 K.

As emphasized in the introduction section, we point to the importance of the TE power factor in addition to the Seebeck coefficient. **Figure 6a** presents the temperature behavior of the power factor for Devices M1 and M9. The power factor always increases with increasing temperature. In particular, the thinner MoS_2 device (Device M1) exhibits a much higher power factor. For the thicker MoS_2 device, the power factor is lower while it increases exponentially with the temperature. The result also indicates a decreasing manner of the power factor with an increase in MoS_2 flake thickness, which will be disclosed in the bottom panel of **Fig. 6b**. In **Fig. 6b**, we provide summarized results of the Seebeck coefficient, the conductivity, and the power factor as a function of the MoS_2 flake thickness with dashed line as guides to eyes, drawn by the least-square fitting. On the upper panel, the Seebeck coefficient increases from ~0.15 mV/K, and it reaches a maximum above 0.3 mV/K for the MoS_2 TE-FET device with a flake thickness of ~20 layers. The Seebeck coefficient turns down afterward, dropping to be less than 0.05 mV/K for the device with a flake thickness of ~40 layers. On the other hand, the middle panel of **Fig. 6b** presents a monotonical decrease in room-temperature conductivity with an increase of the MoS_2 flake thickness. The decreasing trend decelerates for thicker MoS_2 flakes. However, as shown in the lower panel of **Fig. 6b**, the power factor reveals a monotonic decreasing feature with increasing flake thickness for MoS_2 TE-FET devices. The decreasing manner is aggravated for MoS_2 TE-

FET devices with a thickness higher than 30 layers. The Seebeck coefficient and the power factor are all important in energy export. Thus, choosing the MoS_2 with a thickness of less than 20 layers gives the optimum performance for the TE application. **Figure 6c** presents the benchmarking performance of the power factors obtained in the 2D semiconductors. The red star points to the current result of the monolayer MoS_2 TE-FET device, and it points to the power factor of 1.05 mW/m K^2 at room temperature. According to the literature survey, only bilayer WSe_2 and MoS_2 flakes demonstrate power factors higher than the current result. This indicates that the surrounding conditions and passivating materials are important, and few-layer MoS_2 films with a thickness of less than 20 layers could be the best candidate for TE applications among all 2D semiconductors.

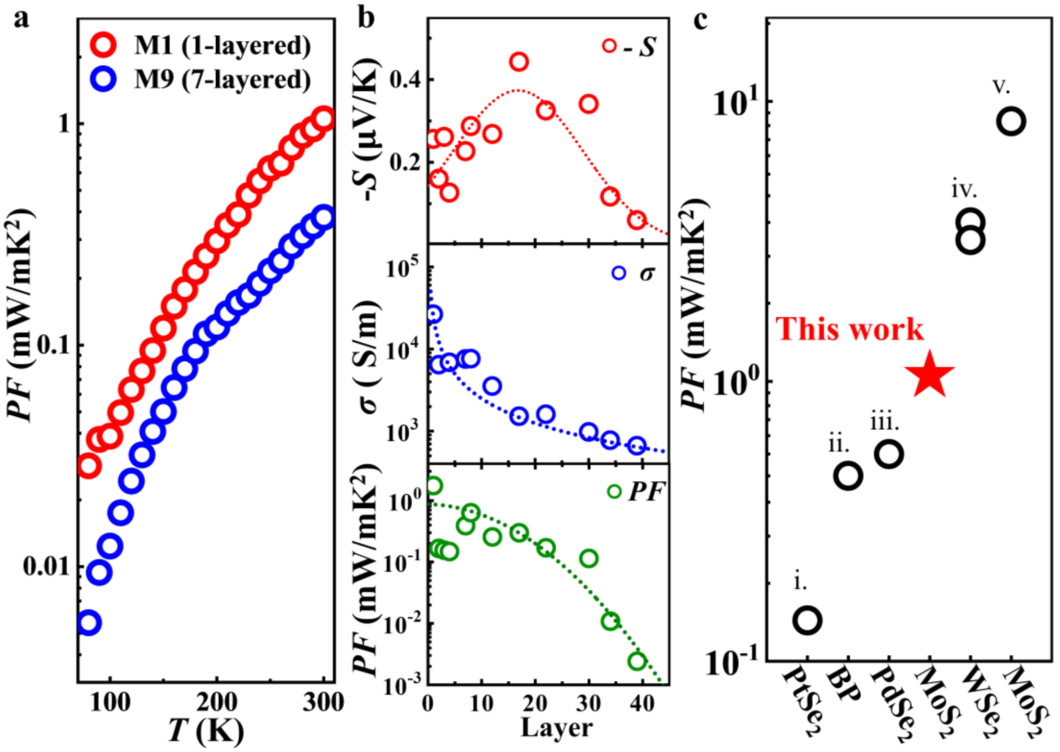

Figure 6. (a) Power factor (PF) in logarithm scale as a function of temperature (in linear scale) of Devices M1 and M9 with thicknesses of 1 and 7 layers at V_{BG} of 60 V. (b) Seebeck coefficient, conductance, and PF as a function of MoS_2 thickness at 300 K. The dashed curves

drawn according to the least-square fitting are guides to eyes. (c) PF of several different 2D materials at room temperature: (i) bilayer $PtSe_2$[38] (ii) 40 nm thick BP flake[39], (iii) 5 nm thick $PdSe_2$ flake[40], (iv) bilayer WSe_2 single crystal flake [41], and (v) bilayer MoS_2 flake[30]. The red star points to the result of this work (Device M1).

Conclusions

Thermopower and electron transport are simultaneously explored in MoS_2 TE-FET devices with thicknesses ranging from monolayer up to 39 layers in a wide temperature range from 80 to 600 K. The electron transport reveals Mott's 2D variable range hopping at temperatures lower than 300 K, thermally activated transport at temperatures ranging from 300 to ~450 K, and phonon scattering at temperatures higher than 460 K. The corresponding Seebeck coefficient, however, presents only Mott's 2D variable range hopping and phonon scattering behaviors as a monotonically increasing feature with increasing temperature. The maximum of the Seebeck coefficient is ~698 μV/K for the tri-layer MoS_2 TE-FET device at 600 K. Particularly, the feature of decreasing manner with an increase in temperature as a symbol of the thermally activated transport has not been discovered yet in all TE-FET devices with different thicknesses. In addition to temperature dependences, the carrier concentration behaviors of the thermally activated energy, the disorder parameter T_0, and the Seebeck coefficients are examined simultaneously to confirm the theories implemented in the wide temperature range. In particular, the Seebeck coefficients as a function of carrier concentration are analyzed separately in either low or high carrier concentrations. In those fittings, the universal constant of k_B/q and the carrier's effective mass have been estimated. The effective mass of electrons in the monolayer MoS_2 is evaluated to be ~0.1 m_0. Moreover, the power factors of the MoS_2 TE-FET devices are measured, and the layer number dependences of the Seebeck coefficient, the conductivity, and the power factor are studied and sketched in diagrams. The power factor of the current work is benchmarked with others' results. It is confirmed that the few-layer MoS_2 films with thicknesses of less than 20 layers could be the best candidates for TE applications. On the other hand, we have explored the extrinsic effect due to trapped electrons in the SiO_2 substrates. The extrinsic effect exists in both electron transport and thermopower for the TE-FET devices at temperatures higher than ~450 K. Very sensitive temperature dependences of the differential of the Seebeck coefficient and the transconductance are discovered. The trapped carrier concentration is evaluated to be $\sim 6.84 \times 10^{11}$ cm^{-2} for the tri-layer MoS_2 TE-FET device at 600 K. The release of the trapped electrons causes an increase in conductivity and current by up to ~45%. It causes a rise in the power factor of ~38% while it decreases the Seebeck coefficient by ~2.5%. The extrinsic effect of trapping charges in the substrate can be applied to thermal sensors at high temperatures.

Experimental Sections

Fabrication of Few-layer MoS_2 TE-FETs. Few-layer MoS_2 flakes were obtained by mechanically exfoliation from a MoS_2 bulk, purchased from Structure Probe, Inc., USA. The few-layer MoS_2 flakes were transferred to a heavily *p*-doped Si wafer, with a resistivity of approximately $0.001\ \mathrm{ohm \cdot cm}$, and capped with 300-nm thick SiO_2 using a high-precision alignment stacking system (HPAS Mono, Nanovie Co. Ltd., Taiwan) and polydimethylsiloxane (PDMS, PF-40-X4, Gel-Pak, USA). A standard electron beam lithography system, including a scanning electron microscope (JSM-IT300, JEOL, Japan) and an electron-beam controller (ELPHY Quantum, Raith GmbH, Germany), was used to pattern contact electrodes. Subsequently, Ti/Au (10 nm/100 nm) metals were deposited by thermal evaporation in a high vacuum of $\sim 3 \times 10^{-6}$ torr. After the lift-off process by acetone, the source, drain and heater electrodes were formed, and the MoS_2 TE-FET devices were manufactured.

Determination of The Thickness of MoS_2 Flake. The thickness of MoS_2 flakes of less than 5 layers was determined using an optical microscope, based on contrast differences in green- and red-color channels. The optical contrast variations with thickness were calibrated by Raman spectroscopy (Shamrock SR500, Andor Technology, Northern Ireland) with laser light of 532 nm in wavelength and spot size of ~1 μm. The details of the calibration are discussed in **Fig. S1** in the **Supporting Information**. The thicknesses of those thicker MoS_2 flakes were measured using an atomic force microscope (AFM, SPA-300HV, Seiko Instruments Inc., Japan) which was operating in a tapping mode. AFM tips (PPP-SEIHR, Nanosensors, Switzerland) with a radius of ~10 nm, a force constant of 15 N/m, and a resonance frequency of 130 kHz were employed for the measurements.

Electrical Characterization. The as-fabricated MoS_2 TE-FET devices are placed in the probe station (TTPX, Lake Shore Cryotronics, Inc., USA) in a high vacuum of $\sim 10^{-6}$ torr. The electrical transport characterizations wer carried out by electrometers of Keithley 6430 and Keithley 2400 (Tektronix, Inc., USA). The Keithley 6430 was used to supply source-drain voltages and acquire currents with preamplifier, and the Keithley 2400 was used to offer the back-gating voltages on the back side of the substrate.

Thermal electrical characterization. The Seebeck coefficients (S) were calculated according to the form $S = -V_{TE}/\Delta T$, where ΔT is a temperature difference and V_{TE} is a thermoelectric voltage. To generate a temperature gradient of ΔT, an AC voltage at the specified frequency of 6.85 Hz was applied on the heater electrode using a function generator (Agilent 33522A, Agilent, USA). Detailed measurements of ΔT are provided in the discussion of **Fig. S2** in the **Supporting Information**. The V_{TE} was determined using the standard 2ω method, recorded by a lock-in amplifier (SR830, Stanford Research Systems, USA) at a frequency of 13.7 Hz. During the measurement, the back-gating voltage was supplied by Keithley 2400 (Tektronix, Inc., USA).

ASSOCIATED CONTENT

Supporting Information. The information of the identification of layer numbers of MoS_2 flakes, device parameters, estimation of temperature gradient for the evaluation of the Seebeck coefficients, temperature dependent resistance at high temperatures, estimation of the k_B/q and the electron effective mass, estimation of trapped charges in the SiO_2, thickness dependences of the differential of the Seebeck coefficient, and thermoelectric parameters of all devices are described in detail in the Supporting Information. This material is available free of charge via the Internet at http://pubs.acs.org.

AUTHOR INFORMATION

Corresponding Authors

*S. S. Islam, Email: sislam@jmi.ac.in

*Wen-Bin Jian, Email: wbjian@nycu.edu.tw

ORCID

Wen-Bin Jian: 0000-0002-1898-9641

Author Contributions

The manuscript was written through contributions of all authors. All authors have given approval to the final version of the manuscript.

ACKNOWLEDGMENT

This work was supported by the National Science and Technology Council, Taiwan, under Grant Nos. NSTC-111-2124-M-A49-008 and NSTC-111-2112-M-A49-038. This work was also financially supported by the "Center for the Semiconductor Technology Research" from The Featured Areas Research Center Program within the framework of the Higher Education Sprout Project by the Ministry of Education, Taiwan, and supported in part by the National Science and Technology Council, Taiwan, under Grant No. NSTC 111-2634-F-A49-008.

REFERENCES

(1) Dresselhaus, N. S.; Chen, G.; Tang, M. Y.; Yang, R.; Lee, H.; Wang, D.; Ren, Z.; Fleurial, J. P.; Gogna, P. New Direction for Low-Dimensional Thermoelectric Materials. *Adv. Mater.* **2007**, *19* (8), 1043-1053.

(2) Minnich, A. J.; Dresselhaus, N. S.; Ren, Z. F.; Chen, G. Bulk Nanostructured Thermoelectric Materials: Current Research and Future Prospects. *Energy Environ. Sci.* **2009**, *2* (5), 466-479.

(3) Goldsmid, H. J. *Thermoelectric Refrigeration*; Plenum Press, New York, 1964.

(4) Takabatake, T.; Suekuni, K. Phonon-Glass Electron-Crystal Thermoelectric Clathrates: Experiments and Theory. *Rev. Mod. Phys.* **2014**, *86* (2), 669-716.

(5) Heremans, J. P.; Jovovic, V.; Toberer, E. S.; Saramat, A.; Kurosaki, K.; Charoenphakdee, A.; Yamanaka, S.; Snyder, G. J. Enhancement of Thermoelectric Efficiency in PbTe by Distortion of the Electronic Density of States. *Science* **2008**, *321* (5888), 554-557.

(6) Cutler, M.; Mott, N. F. Observation of Anderson Localization in an Electron Gas. *Phys. Rev.* **1969**, *181* (3), 1336-1340.

(7) Amollo, T. A.; Mola, G. T.; Kirui, M. S. K.; Nyamori, V. O. Graphene for Thermoelectric Applications: Prospects and Challenges. *Crit. Rev. Solid State Mater. Sci.* **2018**, *43* (2), 133-157.

(8) Wu, J.; Cen, Y.; Wu, J.; Hippalgaonkar, K. Perspectives on Thermoelectricity in Layered and 2D Materials. *Adv. Electron. Mater.* **2018**, *4* (12), 1800248.

(9) Liu, W.; Kim, H. S.; Jie, Q.; Ren, Z. Importance of High Power Factor in Thermoelectric Materials for Power Generation: A Perspective. *Scr. Mater.* **2016**, *111*, 3-9.

(10) Novoselov, K. S.; Geim, A. K.; Morozov, S. V.; Jiang, D.; Zhang, Y.; Dubonos, S. V.; Grigorieva, I. V.; Firsov, A. A. Electric Field Effect in Atomically Thin Carbon Films. *Science* **2004**, *306* (5696), 666–669.

(11) Wang, Q. H.; Kalantar-Zadeh, K.; Kis, A.; Coleman, J. N.; Strano, M. S. Electronics and Optoelectronics of Two-Dimensional Transition Metal Dichalcogenides. *Nat. Nanotechnol.* **2012**, *7* (11), 699–712.

(12) Patil, R. A.; Tu, H. W.; Jen, M. H.; Lin, J. J.; Wu, C. C.; Yang, C. C.; Pham, D. V.; Tsai, C. H.; Lai, C. C.; Liou, Y.; Jian, W. B.; Ma, Y. R. Intriguing Field-Effect-Transistor Performance of Two-Dimensional Layered and Crystalline CrI_3. *Mater. Today Phys.* **2020**, *12*, 100174.

(13) Tu, H. W.; Shih, C. C.; Lin, C. L.; Yu, M. Z.; Lai, J. J.; Luo, J. C.; Lin, G. L.; Jian, W. B.; Watanabe, K.; Taniguchi, T.; Hu, C. High Field-Effect Performance and Intrinsic Scattering in the Two-Dimensional MoS_2 Semiconductors. *Appl. Surf. Sci.* **2021**, *564*, 150422.

(14) Shih, C. C.; Huang, M. H.; Wan, C. K.; Jian, W. B.; Kono, K.; Lin, Y. F.; Ho, C. H. Tuning Interface Barrier in 2D BP/$ReSe_2$ Heterojunctions in Control of Optoelectronic Performances and Energy Conversion Efficiencies, *ACS Photonics* **2020**, *7* (10), 2886-2895.

(15) Radisavljevic, B.; Radenovic, A.; Brivio, J.; Giacometti, V.; Kis, A. Single-Layer MoS_2 Transistors. *Nat. Nanotechnol.* **2011**, *6* (3), 147-150.

(16) Liu, X.; Qu, D.; Ryu, J.; Ahmed, F.; Yang, Z.; Lee, D.; Yoo, W. J. P-Type Polar Transition of Chemically Doped Multilayer MoS_2 Transistor. *Adv. Mater.* **2016**, *28* (12), 2345-2351.

(17) Liu, Y.; Guo, J.; Wu, Y.; Zhu, E.; Weiss, N. O.; He, Q.; Wu, H.; Cheng, H.-C.; Xu, Y.; Shakir, I.; Huang, Y.; Duan, X. Pushing the Performance Limit of Sub-100 nm Molybdenum Disulfide Transistors. *Nano Lett.* **2016**, *16* (10), 6337-6342.

(18) Liu, T.; Liu, S.; Tu, K.-H.; Schmidt, H.; Chu, L.; Xiang, D.; Martin, J.; Eda, G.; Ross, C. A.; Garaj, S. Crested Two-Dimensional Transistors. *Nat. Nanotechnol.* **2019**, *14* (3), 223-226.

(19) Ng, H. K.; Xiang, D.; Suwardi, A.; Hu, G.; Yang, K.; Zhao, Y.; Liu, T.; Cao, Z.; Liu, H.; Li, S.; Cao, J.; Zhu, Q.; Dong, Z.; Tan, C. K. I.; Chi, D.; Qiu, C. W.; Hippalgaonkar, K.;

Eda, G.; Yang, M.; Wu, J. Improving Carrier Mobility in Two-Dimensional Semiconductors with Rippled Materials. *Nat. Electron.* **2022**, *5* (8), 489-496.

(20) Radisavljevic, B.; Kis, A. Mobility Engineering and a Metal–Insulator Transition in Monolayer MoS_2. *Nat. Mater.* **2013**, *12* (9), 815-820.

(21) Ye, J. T.; Zhang, Y. J.; Akashi, R.; Bahramy, M. S.; Arita, R.; Iwasa, Y. Superconducting Dome in a Gate-Tuned Band Insulator. *Science* **2012**, *338* (6111), 1193-1196.

(22) Bertolazzi, S; Krasnozhon, D.; Kis, A. Nonvolatile Memory Cells Based on MoS_2/Graphene Heterostructures. *ACS Nano* **2013**, *7* (4), 3246-3252.

(23) Jiang, C.; Rumyantsev, S. L.; Samnakay, R.; Shur, M. S.; Balandin, A. A. High-Temperature Performance of MoS_2 Thin-Film Transistors: DC and Pulse Current-Voltage Characteristics. *J. Appl. Phys.* **2015**, *117* (6), 064301.

(24) He, G.; Ramamoorthy, H.; Kwan, C.-P.; Lee, Y.-H.; Nathawat, J.; Somphonsane, R.; Matsunaga, M.; Higuchi, A.; Yamanaka, T.; Aoki, N.; Gong, Y.; Zhang, X.; Vajtai, R.; Ajayan, P. M.; Bird, J. P. Thermally Assisted Nonvolatile Memory in Monolayer MoS_2 Transistors. *Nano Lett.* **2016**, *16* (10), 6445-6451.

(25) Kaushik, N.; Mackenzie, D. M. A.; Thakar, K.; Goyal, N.; Mukherjee, B.; Boggild, P.; Petersen, D. H.; Lodha, S. Reversible Hysteresis Inversion in MoS_2 Field Effect Transistors. *npj 2D Mater. Appl.* **2017**, *1* (1), 34.

(26) Buscema, M.; Barkelid, M.; Zwiller, V.; van der Zant, H. S. J.; Steele, G. A.; Castellanos-Gomez, A. Large and Tunable Photothermoelectric Effect in Single-Layer MoS_2. *Nano Lett.* **2013**, *13* (2), 358-363.

(27) Wu, J.; Schmidt, H.; Amara, K. K.; Xu, X.; Eda, G.; Özyilmaz, B. Large Thermoelectricity via Variable Range Hopping in Chemical Vapor Deposition Grown Single-Layer MoS_2. *Nano Lett.* **2014**, *14* (5), 2730-2734.

(28) Babaei, H., Khodadadi, J. M.; Sinha, S. Large theoretical thermoelectric power factor of suspended single-layer MoS_2. *Appl. Phys. Lett.* **2014**, *105* (19), 193901.

(29) Kayyalha, M.; Maassen, J.; Lundstrom, M.; Shi, L.; Chen, Y. P. Gate-Tunable and Thickness-Dependent Electronic and Thermoelectric Transport in Few-Layer MoS_2. *J. Appl. Phys.* **2016**, *120* (13), 134305.

(30) Hippalgaonkar, K.; Wang, Y.; Ye, Y.; Qiu, D. Y.; Zhu, H.; Wang, Y.; Moore, J.; Louie, S. G.; Zhang, X., High Thermoelectric Power Factor in Two-Dimensional Crystals of MoS_2. *Phys. Rev. B* **2017,** *95* (11), 115407.

(31) Wu, J.; Liu, Y.; Liu, Y.; Cai, Y.; Zhao, Y.; Ng, H. K.; Watanabe, K.; Taniguchi, T.; Zhang, G.; Qiu, C. W.; Chi, D.; Neto, A. H. C.; Thong, J. T. L.; Loh, K. P.; Hippalgaonkar, K. Large Enhancement of Thermoelectric Performance in MoS_2/*h*-BN Heterostructure due to Vacancy-Induced Band Hybridization. *Proc. Natl. Acad. Sci. U.S.A.* **2020**, *117* (25), 13929-13936.

(32) Mott, N. F.; Davis, E. A. Electronic Processes in Non-Crystalline Materials, 2nd Ed., Oxford University Press, Oxford, **1979**, pp. 32-35.

(33) Zuev, Y. M.; Chang, W.; Kim, P. Thermoelectric and Magnetothermoelectric Transport Measurements of Graphene. *Phys. Rev. Lett.* **2009**, *102* (9), 096807.

(34) Huang, X.; Yao, Y.; Peng, S.; Zhang, D.; Shi, J.; Jin Z. Effects of Charge Trapping at the MoS_2-SiO_2 Interface on the Stability of Subthreshold Swing of MoS_2 Field Effect Transistors. *Materials* **2020**, *13* (13), 2896.

(35) Burns, M. J.; Chaikin, P. M. Interaction Effects and Thermoelectric Power in Low-Temperature Hopping. *J. Phys. C: Solid State Phys.* **1985**, *18*(24), L743.

(36) Shi, X.; Lu, N.; Xu, G.; Cao, J.; Ham, Z.; Yang, G.; Li, L.; Liu, M. An Analytical Seebeck Coefficient Model for Disordered Organic Semiconductors. *Phys. Lett. A* **2017**, *381*(40), 3441.

(37) Cutler, M.; Leavy, J. F.; Fitzpatrick, R. L. Electronic Transport in Semimetallic Cerium Sulfide. *Phys. Rev.* **1964**, *133*(4A), A1143.

(38) Moon, H.; Bang, J.; Hong, S.; Kim, G.; Roh, J. W.; Kim, J.; Lee, W., Strong Thermopower Enhancement and Tunable Power Factor via Semimetal to Semiconductor Transition in a Transition-Metal Dichalcogenide. *ACS nano* **2019,** *13* (11), 13317-13324.

(39) Saito, Y.; Iizuka, T.; Koretsune, T.; Arita, R.; Shimizu, S.; Iwasa, Y., Gate-Tuned Thermoelectric Power in Black Phosphorus. *Nano Lett.* **2016,** *16* (8), 4819-4824.

(40) Zhao, Y.; Yu, P.; Zhang, G.; Sun, M.; Chi, D.; Hippalgaonkar, K.; Thong, J. T.; Wu, J., Low-Symmetry $PdSe_2$ for High Performance Thermoelectric Applications. *Adv. Funct. Mater.* **2020,** *30* (52), 2004896.

(41) Yoshida, M.; Iizuka, T.; Saito, Y.; Onga, M.; Suzuki, R.; Zhang, Y.; Iwasa, Y.; Shimizu, S., Gate-Optimized Thermoelectric Power Factor in Ultrathin WSe$_2$ Single Crystals. *Nano Lett.* **2016,** *16* (3), 2061-2065.

Insert Table of Contents Graphic and Synopsis Here